iGABASnFR2: Improved genetically encoded protein sensors of GABA

Ilya Kolb[1,2]*, Jeremy P. Hasseman[1,2]*, Akihiro Matsumoto[3,4], Benjamin J. Arthur[1], Yan Zhang[1,5], Arthur Tsang[1,2], Daniel Reep[1,2], Getahun Tsegaye[1,2], Jihong Zheng[1,2], Ronak Patel[1,5], Loren L. Looger[6], Jonathan S. Marvin[1,5], Wyatt L. Korff[1,2], Keisuke Yonehara[3,4], Glenn C. Turner[1,2]†

* Equal contribution

† Correspondence: turnerg@janelia.hhmi.org

Affiliations

1. Janelia Research Campus, Howard Hughes Medical Institute, Ashburn, Virginia, USA
2. Janelia GENIE Project Team, Janelia Research Campus, Howard Hughes Medical Institute, Ashburn, Virginia, USA
3. Department of Gene Function and Phenomics, National Institute of Genetics, Mishima, Japan.
4. Graduate Institute for Advanced Studies, SOKENDAI, Hayama, Japan.
5. Janelia Tool Translation Team, Janelia Research Campus, Howard Hughes Medical Institute, Ashburn, Virginia, USA
6. HHMI, Department of Neurosciences, University of California, San Diego, La Jolla, California, USA

Abstract

Monitoring GABAergic inhibition in the nervous system has been enabled by development of an intensiometric molecular sensor that directly detects GABA. However the first generation iGABASnFR exhibits low signal-to-noise and suboptimal kinetics, making in vivo experiments challenging. To improve sensor performance, we targeted several sites in the protein for near-saturation mutagenesis, and evaluated the resulting sensor variants in a high throughput screening system using evoked synaptic release in primary cultured neurons. This identified a sensor variant, iGABASnFR2, with 4.2-fold improved sensitivity and 20% faster kinetics, and binding affinity that remained in a range sensitive to changes in GABA concentration at synapses. We also identified sensors with an inverted response, decreasing fluorescence intensity upon GABA binding. We termed the best such negative-going sensor iGABASnFR2n, which can be used to corroborate observations with the positive-going sensor. These improvements yielded a qualitative enhancement of in vivo performance, enabling us to make the first measurements of direction selective GABA release in the retina and confirm a longstanding hypothesis for how sensitivity to motion arises in the visual system.

Introduction

Genetically encoded neurotransmitter sensors have significantly advanced neuroscience by enabling direct, real-time monitoring of neurotransmitter dynamics. These tools have facilitated the study of synaptic transmission, input-output relationships within individual neurons, and large-scale network activity. Among these, genetically encoded sensors for GABA are particularly desirable due to the inherent challenges of detecting inhibitory signaling. GABAergic neurotransmission plays a crucial role in shaping neural circuit dynamics and maintaining the balance between excitation and inhibition across the brain. Disruptions in GABAergic signaling have been implicated in neurological and psychiatric disorders, including epilepsy, schizophrenia, and autism, highlighting the importance of developing sensitive tools to study inhibitory transmission (Sohal & Rubenstein 2019).

Although there are other techniques to measure GABA levels in the brain, they are limited in their sensitivity and/or spatiotemporal resolution. Microdialysis allows direct, quantitative measurement of extracellular GABA, even in human patients, but its temporal resolution is restricted to the scale of minutes (van der Zeyden et al. 2008). Electrophysiological approaches, while offering high sensitivity and temporal precision, do not scale to large neuronal populations and cannot independently distinguish GABAergic signaling from other hyperpolarizing currents (Macdonald & Olsen 1994). These limitations underscore the need for improved genetically encoded fluorescent sensors capable of resolving GABA dynamics with greater sensitivity, specificity, and temporal resolution.

We previously developed an intensity-based GABA Sensing Fluorescent Reporter, iGABASnFR, that increases fluorescence in the presence of GABA (Marvin et al. 2019), from here on referred to as iGABASnFR1. Like many sensors (Marvin et al. 2011), this design used a periplasmic binding protein from bacteria as the ligand binding domain, in this case Pf622 from the bacterium *Pseudomonas fluorescens*. A circularly permuted superfolder GFP (cpSFGFP) was then inserted at a site that supports fluorescence changes associated with GABA binding, and the protein was given trafficking sequences to localize it to the membrane. While this sensor enabled optical monitoring of GABAergic activity, its sensitivity and dynamic range remained limited compared to extensively optimized sensors like jGCaMP and iGluSnFR (Zhang et al. 2023; Aggarwal et al. 2023). In neuronal culture, the original iGABASnFR1 exhibited a half-maximal effective concentration (EC_{50}) of ~30 μM and maximal ΔF/F of ~0.6. A binding pocket mutation (F102G) increased the maximal ΔF/F of the sensor but at the cost of an increased EC_{50} and poor membrane localization. As such, the overall performance of iGABASnFR1 was not well-suited for high-resolution, photon-limited imaging applications.

To address these limitations, we used site-directed mutagenesis to engineer two next-generation GABA sensors, iGABASnFR2 and iGABASnFR2n. These sensors exhibit improved sensitivities and affinities for GABA, with positive- and negative-going fluorescence responses, respectively. Here, we describe the development and characterization of these enhanced GABA sensors and demonstrate their application in imaging inhibitory neurotransmission.

Results

Screening for improved variants

The original iGABASnFR1 (Fig. 1a, top) was engineered to increase fluorescence in the presence of GABA, and express robustly in mammalian neurons, making it a valuable addition to the suite of biosensors available to study the brain (Marvin et al. 2019; Looger & Griesbeck 2012; Dong et al. 2022; Yang et al. 2024). However, iGABASnFR1 is a first-generation sensor, with low sensitivity in vivo, particularly in comparison to other sensors such as jGCaMP and iGluSnFR, which have been subjected to multiple generations of engineering. Consequently, we applied the same screening pipeline used to optimize jGCaMP (Wardill et al. 2013; Zhang et al. 2023; Dana et al. 2016) to the task of improving iGABASnFR performance. This pipeline uses field stimulation to evoke activity of cultured primary neurons expressing different sensor variants. Stimulation elicits synaptic release, allowing us to screen for improved sensor performance by measuring response amplitude and kinetics (Fig. 1b), in an experimental setting that approximates in vivo conditions.

Sensor variants were derived by near-saturation mutagenesis of selected sites within the protein, and performance evaluated in a first round of screening. To select improved variants, we jointly optimized for both the ΔF/F of the sensor and its expression levels. Screening for expression was necessary because in our previous effort to engineer iGABASnFR (Marvin et al. 2019), we discovered several mutations, most notably, F102G, that increased the maximal ΔF/F but exhibited expression problems in neurons, with low baseline fluorescence and intracellular aggregates. We quantified the expression levels of different variants by counting the total number of pixels in a well that showed a significant increase in fluorescence during the field stimulation period. These pixels were classified as responsive pixels.

To guide our site-selection efforts, we used the unliganded crystal structure of a preliminary version of iGABASnFR https://www.rcsb.org/structure/6dgv (Marvin et al. 2019), a strategy that worked well for optimizing GCaMP (Akerboom et al. 2009). Specifically, we identified 39 sites to target: 14 near the GABA binding site, 6 at or around the protein hinge area, 10 on the cpSFGFP and 9 at the interface between the two ligand-binding and cpGFP domains (Fig. 1a, bottom).

In the first round of screening, these 39 sites were targeted for mutagenesis, generating 9±5 substitutions at each site (range: 1 to 19) for a total of 3947 variants. Sensor variants were arrayed in 96-well plates, with each plate containing 4 replicate wells of the same variant, and 8 replicate wells of the original iGABASnFR, which served as part of our quality control measures. Each well received 1, 10 and 40 field stimulation pulses separated by 12 ms, and we calculated responses by averaging fluorescence changes over all the responsive pixels in each well. We found 93 mutants with ΔF/F significantly higher than in-plate iGABASnFR1 controls and 22 of those also had a higher fraction of responsive pixels than iGABASnFR, indicating improved expression (Fig. 1c). Interestingly, at least 20 sequence-confirmed mutations, located in 5 different positions - $R168_{Pf}$, $D276_{Pf}$, $T203_{gfp}$, $V150_{gfp}$ and $V272_{Pf}$ - inverted the response of the sensor, making it decrease in fluorescence with field stimulation (number refers to location in the protein domain denoted by subscript, either cpSFGFP or the ligand binding Pf622). However,

none of the inverted sensors exhibited |ΔF/F| greater than that of iGABASnFR. Among them, the $R168_{gfp}P$ mutant was the most promising, with relatively high ΔF/F (0.6x of iGABASnFR) and expression (2x responsive pixels of iGABASnFR; Fig. 1c).

Although we found many marginally improved variants in the first round of screening, there was no clear winner that could be considered to be a major improvement over iGABASnFR. The most sensitive positive-going mutant in the screen was the previously known mutation $F102_{Pf}G$ (ΔF/F 2.5x of iGABASnFR) which was confirmed to have poor expression (0.3x responsive pixels of iGABASnFR). Similarly, the top-expressing mutant in the screen ($L178_{gfp}Y$; 14.8x responsive pixels of iGABASnFR) had only a modest ΔF/F (1.1x of iGABASnFR). Therefore, in the first round of screening, we succeeded in improving ΔF/F and expression separately but not jointly.

Enhancing performance with combinations of single site mutants

We hypothesized that we could generate variants with both improved sensitivity and expression by combining mutations that conveyed each property separately. To test this, the mutations $S99_{Pf}$→A/G/C, $F102_{Pf}$→G/Y, $F104_{Pf}$→Y/H, $R168_{gfp}$→P, $L178_{gfp}$→R/S, and $K253_{Pf}$→I/Y (labeled in Fig. 1d as plus signs) were chosen based on their performance in the first round and combined to create 635 double mutants, which were then screened in a second round. A large percentage of these mutants (49%) did not pass quality control to be considered for further analysis. The majority of these mutants had poor expression, no detectable response to field stimulation, or both. Of the remaining mutants, 52 exhibited improved expression and ΔF/F over iGABASnFR. More importantly, 27 mutants exhibited ΔF/F higher than $F102_{Pf}G$ and expression better than iGABASnFR, suggesting that our hypothesis was correct and the beneficial properties of the mutants could be additive. Interestingly, many of the mutations that improved ΔF/F and expression in positive-going sensors, did the same in negative-going sensors.

Of these variants, the best combination of dynamic range and expression was the mutant iGABASnFR.$S99_{Pf}A$.$F102_{Pf}Y$.$F104_{Pf}Y$.$L178_{gfp}S$, (hereafter iGABASnFR2). The best variant with inverted signal, iGABASnFR.$S99_{Pf}A$.$F104_{Pf}H$.$R168_{gfp}P$ was designated iGABASnFR2n (for negative-going). When we quantified rise time, peak ΔF/F and signal-to-noise, iGABASnFR2 performance was broadly superior to the original across all field stimulation conditions (Figure 2). For 10 action potentials (APs), iGABASnFR2 exhibited a peak ΔF/F 4.2-fold greater than iGABASnFR1 (iGABASnFR2 0.80 ± 0.12; iGABASnFR1 0.19 ± 0.02; p = 6.41e-28 Tukey's HSD post hoc test following one-way ANOVA), and a signal-to-noise ratio (SNR) 3-fold higher (iGABASnFR2 70.5 ± 10.7; iGABASnFR1 23.6 ± 5.7; p = 6.37e-23). Rise times were slightly faster (iGABASnFR2 38 ± 10 ms; iGABASnFR1 47 ± 21 ms; p = 0.13). The negative-going iGABASnFR2n exhibited slightly reduced performance relative to iGABASnFR2, but still achieved a 3.2-fold greater peak ΔF/F (iGABASnFR2n 0.61 ± 0.12; iGABASnFR1 0.19 ± 0.02; p = 2.50e-19), and 30% higher SNR compared to iGABASnFR1 (iGABASnFR2n 30.2 ± 10.0; iGABASnFR1 23.6 ± 5.7; p = 0.06). However, its kinetics were slower, with a rise time of 71 ± 10 ms. These measures clearly indicate that this next generation of GABASnFRs exhibit broadly improved performance in detecting GABA dynamics during synaptic release.

Structure of the iGABASnFR2-GABA complex

To gain some insight into the structure-function relationship of this sensor, we solved the crystal structure of iGABASnFR2 in complex with GABA (Fig. 3). To examine the conformational changes that accompany GABA binding, we compared this new liganded structure with the apo-form of a precursor of the original iGABASnFR (PDB ID 6DGV). Superimposing the structures, using cpGFP as a reference, revealed that the two lobes of the Venus flytrap domain in Pf622 shift closer together to secure GABA in the binding pocket (Fig. 3a). This conformational change resembles those seen in other bacterial periplasmic amino acid-binding proteins (Quiocho & Ledvina 1996).

The hinge region of Pf622, which connects the two lobes, likely plays a key role in allosteric modulation of ligand binding (Telmer & Shilton 2003; Marvin & Hellinga 2001); (Marvin et al. 2019; Planamente et al. 2012; Planamente et al. 2010). Within that hinge region, the F101L mutation, introduced in the original iGABASnFR1 (Marvin et al. 2019), increased binding affinity 10-fold (Fig. 3b). Also in the hinge region, residue S99 forms hydrogen bonds with the OD2 atom of D59 and NE2 atom of Q17, while the S99A mutation in iGABASnFR2 abolishes these interactions, potentially making the hinge region more flexible.

The GABA binding site itself is defined by the side chains of W9, T13, F100, Y102, W202, R205, D228, and Y264 (Fig. 3c). In iGABASnFR2, two mutations near the ligand binding site enhance interactions: F102Y forms a hydrogen bond via its hydroxyl group with D228, which, in turn, makes a hydrogen bond with the GABA amino group. And F104Y, while farther from the binding site, helps position W202 to interact with GABA through van der Waals forces. These likely contribute to the increased affinity for GABA we describe below.

Mutations at the interface between the ligand-binding domain and cpGFP modulate ligand-binding-induced fluorescence changes in many sensors (Akerboom et al. 2009; Zhang et al. 2023; Ding et al. 2014). In iGABASnFR2, the $L178_{gfp}S$ mutation at this interface is likely involved in a hydrogen-bonding network with nearby hydrophilic residues, enhancing the GABA-induced fluorescence change (Supplementary Fig. 1B). The N260A mutation in iGABASnFR1 eliminates side chain hydrogen bonding, removes a cryptic N-linked glycosylation site (N-X-S/T), and enhances protein expression. Another critical mutation, $F145_{gfp}W$, introduced in the original iGABASnFR1 to improve ΔF/F0, interacts directly with the hydroxyl group in the chromophore and surrounding residues.

Interestingly, although the Venus flytrap domain undergoes significant conformational changes upon GABA binding, cpGFP and its flanking linkers (along with up to four adjacent residues) do not show notable conformational changes (Fig. 3a). The structural difference between the unliganded and liganded forms shows a root mean square deviation of only 0.25 Å. This finding contrasts with observations in GCaMP (Zhang et al. 2023; Akerboom et al. 2009; Akerboom et al. 2012), where calcium binding to calmodulin induces substantial conformational changes at the interface, contributing to the large change in fluorescence with this sensor. These differences suggest a potential strategy to further enhance the performance of iGABASnFR2.

Biochemical Characterization

For *in vivo* applications, the effectiveness of the sensor depends on both its affinity for GABA, as well as the kinetics of GABA binding. Sensor affinity should not be so high that it is saturated by tonic levels of GABA in the brain, but should of course be in a range sensitive to the changes in concentration achieved during synaptic release. In mammals, extrasynaptic GABA concentrations lie in the low micromolar range (0.2–2.5 μM (Roth & Draguhn 2012; Glykys & Mody 2007; Lerma et al. 1986; Tossman et al. 1986), while synaptically released GABA can transiently reach low millimolar concentrations (~1.5–3 mM (Roth & Draguhn 2012; Mozrzymas et al. 2003; Barberis et al. 2004). The half-maximal effective concentration (EC_{50}) of iGABASnFR1 when it is expressed on the surface of neurons is 30 μM, so increasing sensor affinity could potentially lead to improved performance *in vivo* without contaminating signal from tonic GABA levels. However, kinetics are also important - the rapid changes in GABA concentration during synaptic release mean that sensor kinetics have to be fast enough to detect the change before GABA concentrations drop back down due to re-uptake and diffusion.

We first determined sensor affinities by titrating GABA concentration while monitoring fluorescence of purified protein. Somewhat surprisingly, purified iGABASnFR2 showed a smaller dynamic range than iGABASnFR1, although its affinity was higher (Fig. 4a; max dF/F0 iGABASnFR2: 0.45, iGABASnFR1: 1.82; EC_{50} iGABASnFR2 = 1.1 μM, iGABASnFR1 = 5.7 μM); and highly selective for GABA over related compounds (Fig. 4 - fig. supp. 1). Previous work with iGluSnFR showed that titrations with purified protein can exhibit different affinity values than when expressed on the membrane of cultured neurons (Aggarwal et al. 2023). The origins of this discrepancy are not clear, however on-cell titrations are closer to the operating environment of the sensor and are likely the more accurate predictor of *in vivo* performance. We found that on cells the half-maximal effective concentration (EC_{50}) of iGABASnFR2 was 6.4 ± 0.21 μM, a 7-fold higher affinity than iGABASnFR1 and 22-fold higher than iGABASnFR.F102$_{Pf}$G (Fig. 4b). So the improved performance we observed likely stems, in part, from this increased on-cell affinity, which nevertheless remains above background levels of GABA measured in the mammalian brain.

We examined sensor kinetics to step changes in GABA concentration using stopped-flow measurements. Relative to iGABASnFR1, the observed reaction rate constants were far greater for both iGABASnFR2 and iGABASnFR2n (Fig. 4c). iGABASnFR1 exhibits biphasic kinetics, with a relatively fast initial change compounded with a much longer phase before sensor saturation is reached (Marvin et al. 2019). In contrast, both iGABASnFR2 and iGABASnFR2n kinetics were accurately captured by fitting with a single exponential function, indicating a less complex relationship between ligand binding and changes in fluorescence (Fig. 4d). Although significantly faster than the first version, the kinetics of iGABASnFR2 and 2n are still slower than iGluSnFR3 (Aggarwal et al. 2023), suggesting further improvements in sensor performance would be possible if kinetics could be accelerated.

The 1p and 2p spectra of all sensors were similar (Fig 4e,f), as were their apparent pKa values (Fig. 4 - fig. supp. 2); additional biophysical properties are reported in Table 1. Overall, both kinetic and thermodynamic observations suggest that iGABASnFR2 and 2n offer a major

improvement in sensing GABA over the previously available sensor. We next tested this by evaluating performance in vivo.

Evaluating Sensor Performance ex vivo

To evaluate indicator performance in vivo, we examined synaptic transmission in the retina. GABAergic inhibition is believed to play a pivotal role in generating direction-selective responses to motion in the retina REF. Direction-selectivity is thought to originate in starburst amacrine cells (SACs), which extend radially symmetric dendrites from a centrally located soma. Inputs to SACs are sprinkled across the entire dendritic arbor, while the outputs are confined to varicosities located near the dendritic tips.

Motion-selectivity is proposed to arise from differential GABA release. Specifically, the hypothesis is that GABA release is stronger when a visual stimulus moves so that excitation sweeps down the dendritic branch from root to tip (centrifugal motion) rather than when it sweeps from tip to root (centripetal motion) (Fig. 5a). The resulting direction-selective inhibition is relayed to direction-selective retinal ganglion cells (DSGCs) through asymmetric synaptic connections (Briggman et al. 2011; Yonehara et al. 2011) (Fig. 5b). By inhibiting DSGC responses to motion in the null direction, SAC inputs ensure that DSGC output is highly selective for motion in the preferred direction, which is subsequently transmitted to the brain.

Notably, the evidence for this centrifugal selectivity has been obtained by electrophysiological membrane potential recording and two-photon Ca^{2+} imaging from starburst cells (Euler et al. 2002; Vaney et al. 2012). Direct evidence for direction-selective GABA release has been lacking, and imaging GABA release from the starburst cell dendrites would provide important confirmation of the origin of retinal direction selectivity.

We virally transfected starburst amacrine cells with iGABASnFR1 or iGABASnFR2, using a Cre-Lox system for cellular specificity. 6-8 weeks after injection, we dissected retinae and performed two-photon imaging, analyzing activity within small fields of view expected to contain multiple release sites on the amacrine cell dendrites.

We first tested whether we could detect responses to light flashes with a 500 μm spot that covered the entire field of view. iGABASnFR1 showed weak but measurable signals to this full-field stimulation, although detecting responses on single trials was challenging. However, when presented with moving dots, the weak signal made it very difficult to detect direction selectivity, even after trial-averaging. By contrast, iGABASnFR2 responses to static flashes were large enough to be detected on single trials, and robust direction-selectivity of GABA release was readily observed in response to motion stimuli.

We quantified the quality of the signals by computing two measures: 1) response amplitude index (RAI), which denotes the light-evoked response strength and 2) response reliability, which reflects trial-to-trial variance (Methods) (Baden et al. 2016). Overall, both the response amplitudes and the reliability of the responses were significantly higher with iGABASnFR2 than with iGABASnFR1 (Fig. 5i,j). In particular, response reliability was much improved in iGABASnFR2 (mean ± SD iGABASnFR2: 0.66 ± 0.14; iGABASnFR: 0.41 ± 0.11), indicating that this sensor reveals activity that previously would have been below detection threshold.

We also examined the signal-to-noise ratio (SNR) of the responses to motion, comparing response amplitude to the variance of signals at baseline. Compared with iGABASnFR1 signals,

iGABASnFR2 signals had significantly higher SNR with both larger signals and lower variance of the baseline (Fig. 5k,l). The improved SNR and higher response reliability across trials resulted in stable motion responses with lower circular variance (CV; Fig. 5m), yielding better direction selectivity measurements overall. Overall, the improved performance of iGABASnFR2 not only enabled us to detect more responses but also provided a more accurate measure of GABA release evoked by visual motion, directly demonstrating that starburst cells release GABA in a direction-selective manner.

Discussion

Here we report an improved GABASnFR, developed using a high throughput mutagenesis and screening pipeline that has previously been used to optimize calcium indicators (Wardill et al. 2013; Dana et al. 2016; Zhang et al. 2023). Despite the fact that only 20% of primary cultured neurons are expected to be inhibitory REF, this pipeline was still capable of identifying improved sensor variants. iGABASnFR2 has a 7-fold increase in affinity for GABA, as well as a 20% increase in kinetics compared to the first generation sensor. Importantly, sensor affinity remains in a range where it is not likely to be saturated by tonic levels of GABA. Additionally, the improved kinetics make it more likely the sensor can capture the rapid changes in GABA concentration that occur at the synaptic cleft as GABA is released and rapidly reuptaken.

The throughput of the screening platform made it possible to target 39 different sites in the protein for saturation mutagenesis. Such an extensive screen was important to get enough coverage that many sites with relatively small improvements could be combined to derive an overall more effective sensor. Of the 39 sites targeted, we found 12 mutations across 6 sites that contributed to improved sensor performance or expression. However, no single mutation produced an especially large improvement in performance. It was particularly challenging to identify single site variants with both strong expression and high signal:noise. Fortunately many of the single site mutations interacted additively when combined. However, it was also the case that many double mutant combinations failed to pass our basic quality control standards, which may indicate that the combinations resulted in a failed, non-fluorescent sensor. Whether higher-order combinations can realistically yield sensors with improved performance remains an open question—functional variants may prove even more rare when more mutations are combined, and/or the increase in performance may come in smaller increments as higher order combinations are produced.

No single mutation produced an especially large improvement in performance. Identifying single-site variants with both strong expression and high signal-to-noise was particularly challenging. Many of the single-site mutations interacted additively when combined. Still, numerous double mutant combinations failed to pass basic quality control standards, possibly indicating that the combinations produced non-functional, non-fluorescent sensors. Whether higher-order combinations can realistically yield sensors with improved performance remains an open question—functional variants may become even rarer as more mutations are added, and any performance gains may diminish with each additional layer of complexity.

The extensive screening also enabled the serendipitous discovery of negative-going sensors. Of course positive- and negative-going variants cannot be combined in a single experiment

because they are the same color. However, in experiments where precisely timed GABA release is expected, replicating an observation with sensors of different polarities could increase confidence in a result, especially given that signal:noise remains below that of other sensors such as GCaMP and iGluSnFR.

There are several promising avenues that could be taken to further optimize iGABASnFR. First, although several sites contributed small improvements in sensor performance, we did not attempt to go much beyond two-site combinations in this study, so higher order combinations are one straightforward route to further optimization. Second, sensor expression is evidently an aspect which could be improved. We attempted to capture this in our screening criteria by measuring the fraction of responsive pixels for each variant. However this partly conflates the amplitude of the sensor's signal with its expression level, and a more direct measure of expression would be preferable. Thirdly, trafficking the sensor efficiently to the membrane is likely another point of improvement. In work with iGluSnFR (Aggarwal et al. 2023) and eLACCO (Nasu et al. 2023), a panel of different transmembrane anchors were evaluated for sensor localization, and some were found to be more effective than the PDGFR domain that anchors iGABASnFR2. Finally, the high throughput of our screening pipeline may provide sufficient training data that machine learning approaches used to further optimize jGCaMP8 (Wait et al. 2024) can be applied to iGABASnFR.

Nevertheless the improvements we identified yielded a qualitative difference in the ability to detect inhibition in the retina. Although the first-generation sensor showed some signal, direction-selective inhibition was reliably detectable on single trials only with iGABASnFR2. iGABASnFR2 has also been used to detect inhibitory transmission during epileptiform activity in hippocampal slices (Magloire et al. 2023). However it remains untested whether this sensor has the sensitivity to reveal transmission at release sites *in vivo* in the central brain. The iterative evolution of sensors like jGCaMP and iGluSnFR suggests that signal-to-noise will likely need to be improved to detect release at single synapses in vivo (Zhang et al. 2023; Aggarwal et al. 2023). However, the sensor seems very well-suited to less sensitive in vivo applications, where it is possible either to integrate stronger underlying signals than single release events, or to average signals over space, as in photometry experiments. Given the challenges of monitoring inhibitory signaling in the nervous system, we expect that these improved sensors that directly detect GABA release will be valuable tools for the neuroscience community.

Methods

Animal care and use statement

All surgical and experimental procedures involving animals were performed in accordance with protocols approved by the Institutional Animal Care and Use Committee at the respective institute (HHMI Janelia Research Campus, National Institute of Genetics). Procedures in the United States conform to the National Institutes of Health (NIH) Guide for the Care and Use of Laboratory Animals. Procedures in Japan were approved by the animal experimentation committee at the National Institute of Genetics. Mice were housed under controlled temperature (roughly 21°C) and humidity (roughly 50%) conditions under a reverse light cycle. This research has complied with all applicable ethical regulations.

Mutagenesis

Site-directed mutagenesis was carried out using overlapping PCR amplicons with degenerate oligonucleotide primers (NNS). A single-site NNS library (n=96) was created for each amino acid residue of interest and cloned using Gibson assembly. Subsequently, top single-site variants (12 mutations across 6 AA sites) were assembled using overlapping amplicons to achieve all possible combinations of mutations (n= 635 sequence verified variants). For neuronal screening, iGABASnFR variants were cloned into an expression vector containing the CAG promoter, the variant of interest, and finally a woodchuck hepatitis virus post-transcriptional regulatory element (WPRE).

Neuronal cell culture

The primary rat culture procedure was performed largely as previously described (Dana et al. 2016; Wardill et al. 2013). Briefly, neonatal rat pups (Charles River Laboratory) were euthanized and neocortices were dissociated and processed to form a cell pellet. Cells were resuspended and transfected by combining $5x10^5$ viable cells with 400 ng plasmid DNA and nucleofection solution in a 25 µL electroporation cuvette (Lonza). Electroporation of iGABASnFR mutants was performed according to the manufacturer's protocol. Typically, 8 wells in a 96-well plate were electroporated with iGABASnFR1 control, and 18 different mutants were electroporated into 4 wells each for a total of 80 wells. The first and last columns of the plate were not used because pilot experiments indicated that cells grown in these wells exhibited poor health.

Field stimulation assay

The field stimulation assay was adapted from our existing GECI screening pipeline (Dana et al. 2016; Dana et al. 2019). Neurons were plated onto poly-D-lysine-coated, 96-well, glass bottom plates (MatTek) at ~$1x10^5$ cells per well in 100 µL of a 1:4 mixture of NbActiv4 (BrainBits) and plating medium (28 mM glucose, 2.4 mM NaHCO3, 100 µg/mL transferrin, 25 µg/mL insulin, 2 mM L-glutamine, 100 U/mL penicillin, 10 µg/mL streptomycin, 10% FBS in MEM), and placed in an incubator at 37˚C and 5% CO_2. On the following day, 190 µL of NbActiv4 medium was added to each well, and incubation continued for a total of 12-15 days.

For imaging, neuronal culture growth medium was exchanged three times with imaging buffer (145 mM NaCl, 2.5 mM KCl, 10 mM glucose, 10 mM HEPES pH 7.4, 2 mM CaCl2, 1 mM MgCl2) and imaged in 75 µL of imaging buffer and drugs (10 µM CNQX, 10 µM (R)-CPP, 10 µM gabazine, 1 mM (S)-MCPG, Tocris). Fluorescence time-lapse images were collected on an Olympus IX81 microscope using a 10x 0.4 NA objective (UPlanSApo, Olympus) and an ET-GFP filter cube (Chroma #49002). Illumination was provided by a 470 nm LED (Cairn Research) and fluorescence was collected by an EMCCD camera (Ixon Ultra DU897, Andor) with 256 x 256 pixel frames taken at 50 Hz, with 2x binning, over a 0.8 mm x 0.8 mm FOV. A custom platinum electrode was lowered into each well via a linear actuator and neurons were stimulated (1, 10, 40 pulses at 83 Hz, 40 V, 1 ms pulse duration; S-48, Grass Instruments) as time-lapse imaging was performed.

The time-lapse images were analyzed to quantify the responses of the mutants to electrical stimulation. Photobleaching was corrected by fitting a single exponential to the beginning and end of the recording (avoiding the response window). For each pixel in the movie, a Mann-Whitney U test was performed between 1.5 sec preceding the field stimulation and 0.4

sec afterwards. Pixels with a *p*-value < 0.01 for any of those tests were considered to be responsive. The number of responsive pixels was used as a proxy for sensor expression. In the screening phase, measurements of sensitivity (ΔF/F) and kinetics were performed on pooled responsive pixels from each plate, and wells with < 4 responsive pixels were discarded. To account for batch variability, the response of each construct was normalized to the in-plate iGABASnFR1 control.

Quality control on every plate was first performed by visual inspection, examining images from each well and rejecting plates and constructs with aberrantly low expression, significant clumps of unhealthy cells, or other undesirable phenomena. Overall, 54 plates did not pass this initial quality control step, and were re-screened. Subsequently, all constructs with < 1,800 responsive pixels per plate (representing 0.6% of all pixels) were eliminated from analysis.

Protein expression and purification

iGABASnFR variants of interest were expressed in *E. coli* T7 Express cells (New England BioLabs) in 100 mL cultures, pelleted by centrifugation, and frozen overnight. Cells were lysed by resuspending in buffer containing 20% v/v B-PER (ThermoFisher) and 0.2 mg/mL lysozyme. Lysate was sonicated, clarified by centrifugation, and purified using immobilized metal affinity chromatography on 1 mL nickel-charged HisPur resin (ThermoFisher). The protein was eluted in a buffer containing 100 mM imidazole and concentrated by spin concentrator (Amicon).

Crystal structure determination

All crystallization trials were carried out at room temperature using the hanging-drop vapor diffusion method. Commercial sparse-matrix screening solutions were used in initial screens (Hampton Research). 1 μL of protein solution containing 10 mg/mL of iGABASnFR2, 2 mM GABA, 20 mM Tris, 136 mM NaCl, pH 7.4 was mixed with 1 μL of reservoir solution and equilibrated against 250 μL reservoir solution. The reservoir solution for the optimized conditions contained 0.2 M ammonium formate and 20% w/v polyethylene glycol 3350. Diffraction data were collected at the beamline 8.2.1 at Berkeley Center for Structural Biology and processed with XDS (Kabsch 2010). The phase was determined by molecular replacement using MOLREP and the structure of unliganded iGluSnFR precursor (PDB 6DGV) without residue 1-98, 230-248, and 358-376 as the starting model. Subsequently the model was rebuilt with Buccaneer (Cowtan 2006). Refinement was performed using REFMAC, followed by manual remodeling with Coot (Emsley et al. 2010). Details of the crystallographic analysis and statistics are presented in Fig. 3 Supplementary Table 1.

Affinity measurements

Equilibrium binding affinities were determined by titration with serial dilutions of GABA up to 10mM into 0.2 μM protein solution in PBS. Measurements were made on a Tecan Spark plate reader using 490 nm excitation and 515 nm excitation at room temperature (22 °C). The fluorescence data was fitted to the Hill function in GraphPad Prism to determine affinity values.

pH titrations

Fluorescence intensities as a function of pH were measured in both glutamate-saturated (10 mM) and glutamate-free states, and fitted with a sigmoidal binding function to determine the apparent pKa and apparent ΔF/F as a function of pH. The sigmoidal binding function used was

fit using Graphpad Prism v.10 software: F = Fmin + (Fmax−Fmin)/(1+10^(pKa−pH)), where F is the observed brightness, the parameters Fmax and Fmin are limit brightnesses at high and low pH, and pKa is the apparent pKa of the indicator.

On-cell affinity measurements in neuronal culture

To measure the EC_{50} of different sensor variants in culture conditions, neurons were transfected and plated in glass-bottom 24-well plates (Mattek) as described above. After 7 days in culture, they were imaged using a 20× 0.45 NA objective (LUCPlanFL N, Olympus). GABA was perfused into each well using a custom 3D-printed part that held an inlet and outlet perfusion tube. The inlet tube was connected to a 4-channel gravity perfusion system (VC3, ALA Scientific), and the outlet tube was connected to a vacuum trap. Increasing concentrations of GABA from 0.1 μM to 10 mM were perfused into the culture for 5 s, followed by 9 s of GABA-free buffer, as imaging was performed.

Stopped-flow kinetic measurements

GABA binding kinetics were measured using an Applied Photophysics SX20 stopped-flow spectrometer by rapidly mixing equal volumes of dilute purified sensor protein with varying GABA concentrations in PBS buffer. Fluorescence changes were detected using 490 nm excitation and a 515 nm long pass filter. Measurements were taken at room temperature (22 °C). Three replicate measurements were performed for each set of conditions, and reaction traces were fitted to a monoexponential function in Matlab.

One-photon photophysical measurements

All measurements were performed on solutions of purified protein (1 to 5 μM) in 1X PBS (pH 7.3) with 0 mM (apo) and 10 mM (sat) added GABA. Absorbance measurements were performed using UV-Vis spectrometer (Cary 100, Agilent technologies) and fluorescence excitation-emission spectra were measured using a fluorescence spectrometer (Cary Eclipse, Varian Inc.). Excitation scans ranged from 250 to 530 nm and emission scans performed from 470 to 700 nm. ΔF/F, defined as difference in fluorescence from proteins +/- 10 mM GABA, was calculated from the fluorescence emission spectra. Quantum yield measurements were performed via the relative method, using fluorescein dye (QY = 0.90 in 0.1M NaOH) as a reference. Extinction coefficient measurements were determined using the alkali denaturation method, using the extinction coefficient of denatured GFP as a reference (ε = 44000 M-1 cm-1 at 447 nm).

Two-photon measurements

Two-photon excitation spectra were measured as previously described (Akerboom et al. 2012). Protein solutions (1 to 5 μM) +/- 10 mM GABA were prepared and measured using an inverted microscope (IX81, Olympus) equipped with a 60× 1.2 NA water immersion objective (Olympus). Two-photon excitation was achieved using an 80 MHz Ti-Sapphire laser (Chameleon Ultra II, Coherent) for spectra from 710 nm to 1080 nm. Fluorescence collected through the objective was passed through a short pass filter (720SP, Semrock) and a band pass filter (550BP200, Semrock), before being detected by a fiber-coupled Avalanche Photodiode (APD) (SPCM_AQRH-14, Perkin Elmer). The obtained two-photon excitation spectra were normalized for 1 μM concentration and further used to obtain action cross-section spectra (AXS) with fluorescein as a reference (Average AXS from (Xu & Webb 1996; Makarov et al. 2008).

Imaging direction-selective activity in the retina

We injected AAVs encoding iGABASnFR1 (ssAAV-1/2-hSyn-FLEX.iGABASnFR.F102G) and iGABASnFR2.0 (ssAAV-9/2-hSyn1-dlox-iGABASnFR2(rev)-dlox-WPRE-SV40p(A)) into ChAT-IRES-Cre mice to monitor the activity of starburst amacrine cells. 6-8 weeks after injection, we dissected retinae and performed two-photon imaging.

We used two types of visual stimuli: 1) Static flash: a spot with 500 μm diameter, 100% contrast, 2s duration (Fig. 2d,g); 2) Moving spot, a spot with 500 μm diameter, 800 μm/s (Fig. 2e,h).

To quantify the response amplitude, we computed response amplitude index (RAI):

$$RAI = (r_s - r_b)/(r_s + r_b)$$

where r_s denotes the peak ΔF/F0 during visual stimulation and r_b is the mean ΔF/F0 before stimulation.

To evaluate the response reliability, we examine the trial-to-trial variance of the signals (Baden et al. 2016),

$$Var[\langle C\rangle_r]_t/\langle Var[C]_t\rangle_r$$

where C is a matrix constructed of response ΔF(t) in all stimulus trials, and $\langle\rangle_x$ and $Var[]_x$ denote the mean and variance across the indicated dimension x. If all responses are identical across all stimulus trials, reliability is equal to 1.

The signal-to-noise ratio (SNR) of motion responses was quantified as the response strength relative to the variance in baseline,

$$SNR = (R_p - SD_b)/(R_p + SD_b)$$

where R_p denotes response amplitude in the preferred direction and SD_b is the standard deviation of the signal before stimulation.

The circular variance (CV) is computed to quantify directional tuning:

$$CV = \left|(\Sigma_d R_d e^{i2\theta_d})/(\Sigma_d R_d)\right|$$

where R_d denotes response in direction d, and θ_d denotes angle in direction d.

Statistics and reproducibility

Values and errors reported throughout the text are mean ± s.e.m. unless otherwise noted. Statistical analyses were performed in Graphpad Prism v.8 (in vitro photophysics) and MATLAB (others), as described in the text.

Reagent availability

A variety of mammalian and bacterial expression plasmids as well as AAVs for iGABASnFR2 and iGABASnFR2n are available through Addgene (https://www.addgene.org/browse/article/28247749/). Requests for other reagents, such as

sensor variants with different affinities, can be made by contacting GENIEreagents@janelia.hhmi.org.

Acknowledgements:

We thank Tim Brown from the Janelia Tool Translation Team, Deepika Walpita and Phuong Nguyen for providing resources. Work at Janelia research campus was funded by the Howard Hughes Medical Institute. A.M. was supported by funding from PRESTO JST (JPMJPR2489) and KAKENHI (23K19412). K.Y. was supported by funding from KAKENHI (20K23377; 22K21353; 23H04241; 24H02311).

References

Aggarwal, A. et al., 2023. Glutamate indicators with improved activation kinetics and localization for imaging synaptic transmission. *Nature methods*, pp.1–10.

Akerboom, J. et al., 2009. Crystal structures of the GCaMP calcium sensor reveal the mechanism of fluorescence signal change and aid rational design. *The Journal of biological chemistry*, 284(10), pp.6455–6464.

Akerboom, J. et al., 2012. Optimization of a GCaMP calcium indicator for neural activity imaging. *The Journal of neuroscience: the official journal of the Society for Neuroscience*, 32(40), pp.13819–13840.

Baden, T. et al., 2016. The functional diversity of retinal ganglion cells in the mouse. *Nature*, 529(7586), pp.345–350.

Barberis, A., Petrini, E.M. & Cherubini, E., 2004. Presynaptic source of quantal size variability at GABAergic synapses in rat hippocampal neurons in culture. *The European journal of neuroscience*, 20(7), pp.1803–1810.

Briggman, K.L., Helmstaedter, M. & Denk, W., 2011. Wiring specificity in the direction-selectivity circuit of the retina. , 471(7337), pp.183–188.

Cowtan, K., 2006. TheBuccaneersoftware for automated model building. 1. Tracing protein chains. *Acta crystallographica. Section D, Biological crystallography*, 62(9), pp.1002–1011.

Dana, H. et al., 2019. High-performance calcium sensors for imaging activity in neuronal populations and microcompartments. *Nature Publishing Group*, 16(7), pp.649–657.

Dana, H. et al., 2016. Sensitive red protein calcium indicators for imaging neural activity. *eLife*, 5. Available at: http://dx.doi.org/10.7554/eLife.12727.

Ding, J. et al., 2014. Structural basis of the ultrasensitive calcium indicator GCaMP6. *Science China. Life sciences*, 57(3), pp.269–274.

Dong, C. et al., 2022. Fluorescence Imaging of Neural Activity, Neurochemical Dynamics, and Drug-Specific Receptor Conformation with Genetically Encoded Sensors. *Annual review of*

neuroscience, 45, pp.273–294.

Emsley, P. et al., 2010. Features and development of Coot. *Acta Crystallographica Section D: Biological Crystallography*, 66(4), pp.486–501.

Euler, T., Detwiler, P.B. & Denk, W., 2002. Directionally selective calcium signals in dendrites of starburst amacrine cells. *Nature*, 418(6900), pp.845–852.

Glykys, J. & Mody, I., 2007. The main source of ambient GABA responsible for tonic inhibition in the mouse hippocampus: The main source of ambient GABA. *The journal of physiology*, 582(Pt 3), pp.1163–1178.

Kabsch, W., 2010. XDS. *Acta crystallographica. Section D, Biological crystallography*, 66(Pt 2), pp.125–132.

Lerma, J. et al., 1986. In vivo determination of extracellular concentration of amino acids in the rat hippocampus. A method based on brain dialysis and computerized analysis. *Brain research*, 384(1), pp.145–155.

Looger, L.L. & Griesbeck, O., 2012. Genetically encoded neural activity indicators. *Current opinion in neurobiology*, 22(1), pp.18–23.

Macdonald, R.L. & Olsen, R.W., 1994. GABAA receptor channels. *Annual review of neuroscience*, 17(1), pp.569–602.

Magloire, V. et al., 2023. Volume-transmitted GABA waves pace epileptiform rhythms in the hippocampal network. *Current biology: CB*, 33(7), pp.1249–1264.e7.

Makarov, N.S., Drobizhev, M. & Rebane, A., 2008. Two-photon absorption standards in the 550-1600 nm excitation wavelength range. *Optics express*, 16(6), pp.4029–4047.

Marvin, J.S. et al., 2019. A genetically encoded fluorescent sensor for in vivo imaging of GABA. *Nature methods*, 16(8), pp.763–770.

Marvin, J.S. et al., 2011. A genetically encoded, high-signal-to-noise maltose sensor. *Proteins*, 79(11), pp.3025–3036.

Marvin, J.S. & Hellinga, H.W., 2001. Manipulation of ligand binding affinity by exploitation of conformational coupling. *Nature structural biology*, 8(9), pp.795–798.

Mozrzymas, J.W. et al., 2003. Modulation of GABA(A) receptors by hydrogen ions reveals synaptic GABA transient and a crucial role of the desensitization process. *The Journal of neuroscience: the official journal of the Society for Neuroscience*, 23(22), pp.7981–7992.

Nasu, Y. et al., 2023. Lactate biosensors for spectrally and spatially multiplexed fluorescence imaging. *Nature communications*, 14(1), p.6598.

Planamente, S. et al., 2010. A conserved mechanism of GABA binding and antagonism is revealed by structure-function analysis of the periplasmic binding protein Atu2422 in Agrobacterium tumefaciens. *The journal of biological chemistry*, 285(39), pp.30294–30303.

Planamente, S. et al., 2012. Structural basis for selective GABA binding in bacterial pathogens: Structure and function of a selective GABA sensor. *Molecular microbiology*, 86(5),

pp.1085–1099.

Quiocho, F.A. & Ledvina, P.S., 1996. Atomic structure and specificity of bacterial periplasmic receptors for active transport and chemotaxis: variation of common themes. *Molecular microbiology*, 20(1), pp.17–25.

Roth, F.C. & Draguhn, A., 2012. GABA metabolism and transport: effects on synaptic efficacy. *Neural plasticity*, 2012, p.805830.

Sohal, V.S. & Rubenstein, J.L.R., 2019. Excitation-inhibition balance as a framework for investigating mechanisms in neuropsychiatric disorders. *Molecular psychiatry*, 24(9), pp.1248–1257.

Telmer, P.G. & Shilton, B.H., 2003. Insights into the conformational equilibria of maltose-binding protein by analysis of high affinity mutants. *The journal of biological chemistry*, 278(36), pp.34555–34567.

Tossman, U., Jonsson, G. & Ungerstedt, U., 1986. Regional distribution and extracellular levels of amino acids in rat central nervous system. *Acta physiologica Scandinavica*, 127(4), pp.533–545.

Vaney, D.I., Sivyer, B. & Taylor, W.R., 2012. Direction selectivity in the retina: symmetry and asymmetry in structure and function. *Nature reviews. Neuroscience*, 13(3), pp.194–208.

Wait, S.J. et al., 2024. Machine learning-guided engineering of genetically encoded fluorescent calcium indicators. *Nature computational science*, 4(3), pp.224–236.

Wardill, T.J. et al., 2013. A Neuron-Based Screening Platform for Optimizing Genetically-Encoded Calcium Indicators. *PloS one*, 8(10), p.e77728.

Xu, C. & Webb, W.W., 1996. Measurement of two-photon excitation cross sections of molecular fluorophores with data from 690 to 1050 nm. *Journal of the Optical Society of America. B, Optical physics*, 13(3), p.481.

Yang, Y., Li, B. & Li, Y., 2024. Genetically encoded sensors for the in vivo detection of neurochemical dynamics. *Annual review of analytical chemistry (Palo Alto, Calif.)*, 17(1), pp.367–392.

Yonehara, K. et al., 2011. Spatially asymmetric reorganization of inhibition establishes a motion-sensitive circuit. *Nature*, 469(7330), pp.407–410.

van der Zeyden, M. et al., 2008. Microdialysis of GABA and glutamate: analysis, interpretation and comparison with microsensors. *Pharmacology, biochemistry, and behavior*, 90(2), pp.135–147.

Zhang, Y. et al., 2023. Fast and sensitive GCaMP calcium indicators for imaging neural populations. *Nature*, 615(7954), pp.884–891.

Figure Legends

Figure 1. Field stimulation screen for improved iGABASnFR.

a. Top: Schematic representation of iGABASnFR1 and the amino acid substitutions that gave rise to iGABASnFR2 and iGABASnFR2n. White, IgG secretion signal (cleaved off during trafficking to cell surface); blue, GABA binding protein Pf622; green, cpSFGFP; dark green, Myc epitope tag; red, PDGFR transmembrane domain. Numbering is relative to each of the constituent protein domains; the relationship to sequential numbering of the entire polypeptide is shown in **Figure 1 - figure supplement 1**.

Bottom: Crystal structure of a preliminary version of iGABASnFR (PDB ID 6DGV) with the 39 sites targeted for mutagenesis. Gray spheres indicate the approximate position of GABA, based on homology to the liganded structure of GABA-binding protein Atu4243 (Planamente et al. 2012).

b. Mutagenesis and screening strategy. Variants with single site mutations are screened for ΔF/F and expression in an initial field stimulation assay, strong performers identified and then combined and re-screened in a second round. The top-performing mutants (positive-going quadruple mutant iGABASnFR2 and negative-going triple mutant iGABASnFR2n) are characterized further.

c. Joint optimization of sensitivity (ΔF/F, x-axis) and expression, measured with responsive pixels (y-axis). ΔF/F is normalized to in-plate iGABASnFR1 controls. Black circle: (1,1) position represents iGABASnFR. Plus signs: mutants from the first round that were put together to form combos in the second round. iGABASnFR2 and 2n exhibited increased ΔF/F (4.3-fold and -2.2-fold of iGABASnFR, respectively) and greater numbers of responsive pixels (13.1-fold and 10.3-fold). Illumination: 0.34 mW/mm^2, imaging framerate: 50 Hz.

d. Performance measures of sensor variants from the screen. Single site variants shown in gray, double site combinations shown in black. Variants are ranked according to the ΔF/F0 values measured for 40 AP, and those rankings maintained for the lower displays of sensor F0, tau on, the time constant of the rising phase of the response, and tau off for the decay. All values are normalized to in-plate iGABASnFR1 controls.

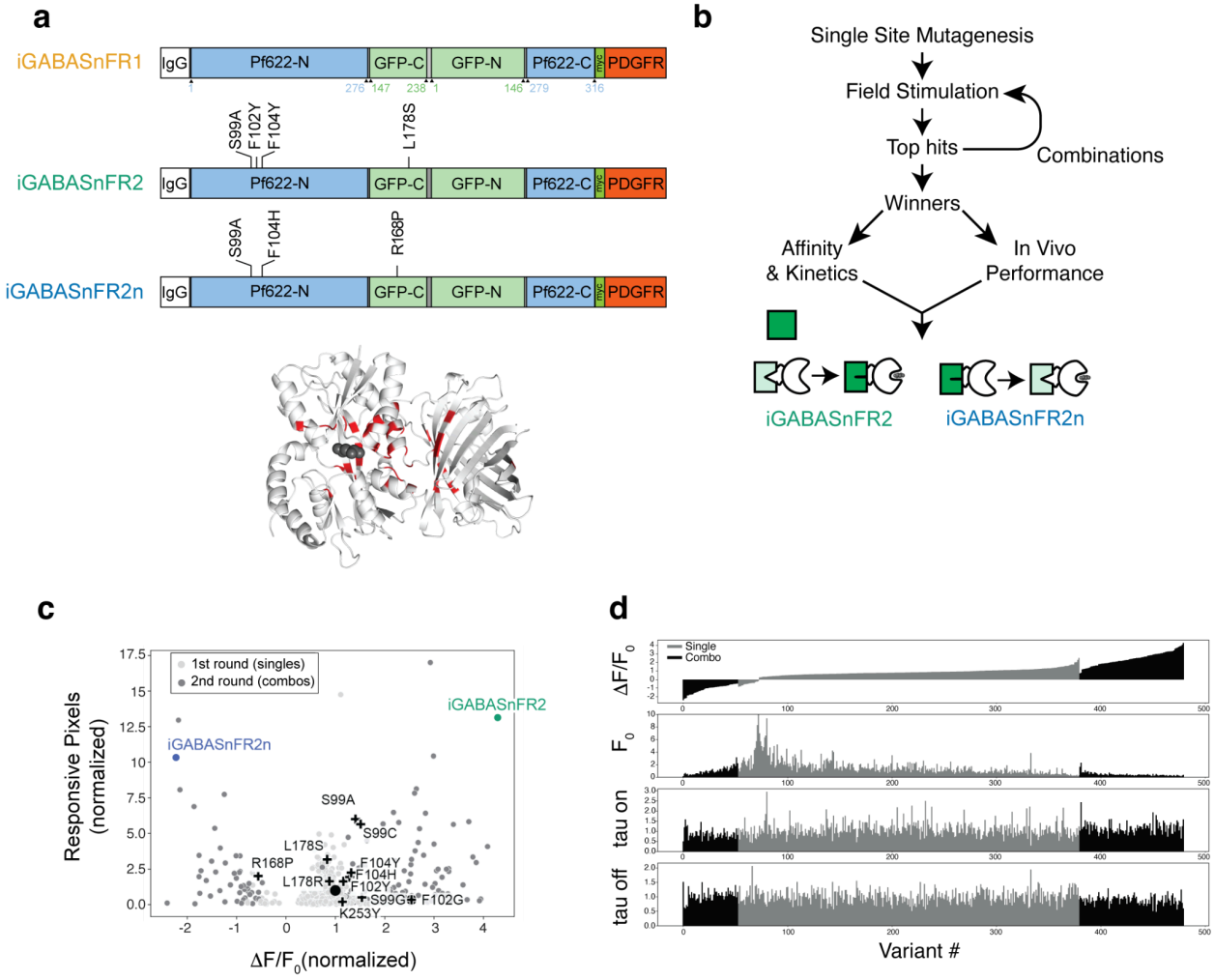
a
iGABASnFR1
IgG
Pf622-N
GFP-C
GFP-N
Pf622-C
TM
PDGFR
1
276
147
238
1
146
279
316
S99A
F102Y
F104Y
L178S
iGABASnFR2
S99A
F104H
R168P
iGABASnFR2n
b
Single Site Mutagenesis
Field Stimulation
Top hits
Combinations
Winners
Affinity
& Kinetics
In Vivo
Performance
iGABASnFR2
iGABASnFR2n
c
1st round (singles)
2nd round (combos)
iGABASnFR2
iGABASnFR2n
S99A
S99C
L178S
R168P
F104Y
F104H
L178R
F102Y
S99G
F102G
K253Y
Responsive Pixels
(normalized)
ΔF/F0(normalized)
d
Single
Combo
ΔF/F0
F0
tau on
tau off
Variant #

Figure 1 - figure supplement 1.

a. Annotated amino acid sequence of iGABASnFRs. iGABASnFR1 sequence shown in gray text, with sites targeted for mutagenesis in black.

Shading indicates domains according to:
IgG secretion signal
Pf622 2-276
SFGFP 147-238 Junction SFGFP 1-146
Pf622 277-320
Myc epitope
PDGFR transmembrane domain 513-561

b. iGABASnFR2 sequence, with mutations shown in red text. Mutations are listed according to domain numbers, with sequential numbering through the polypeptide indicated at the left.

Sequential numbering through the polypeptide is indicated on the left, while mutations in the text are listed according to domain numbers: $S99_{Pf}A.F102_{Pf}Y.F104_{Pf}Y.L178_{gfp}S$.

$S99_{Pf}A.F102_{Pf}Y.F104_{Pf}Y.L178_{gfp}S$, which we subsequently refer to as iGABASnFR2, and the best variant with inverted signal, iGABASnFR.$S99_{Pf}A.F104_{Pf}H.R168_{gfp}P$ was chosen to be iGABASnFR2n

c. iGABASnFR2n sequence, with mutations shown in red text. Sequential numbering through the polypeptide is indicated on the left, while mutations in the text are listed according to domain numbers: $S99_{Pf}A.F104_{Pf}H.R168_{gfp}P$.

d. Schematic showing the relationship between domain-based numbering scheme and sequential numbering through the entire polypeptide (top) and the domain-based numbering scheme. In both schemes numbering starts at the residue exposed after signal sequence cleavage.

IgG secretion signal
Pf622 2-276
SFGFP 147-238 Linker SFGFP 1-146
Pf622 277-320
Myc epitope
PDGFR transmembrane domain 513-561

iGABASnFR1

```
  1 METDTLLLWV LLLWVPGSTG DRSESINFVS WGGSTQDAQK QAWADPFSKA SGITVVQDGP
 61 TDYGKLKAMV ESGNVQWDVV DVEADFALRA AAEGLLEPLD FSVIQRDKID PRFVSDHGVG
121 SFLFSFVLGY NEGKLGASKP QDWTALFDTK TYPGKRALYK WPSPGVLELA LLADGVPADK
181 LYPLDLDRAF KKLDTIKKDI VWWGGGAQSQ QLLASGEVSM GQFWNGRIHA LQEDGAPVGV
241 SWKQNLVMAD ILVVPKGTKN KAAAMKFLAS ASSAKGQDDF SALTAYAPVN IDSVQRLDLA
301 QVRITADKQK NGIMANFKIR HNVEDGSVQL ADHYQQNTPI GDGPVLLPDN HYLSTQSVLS
361 KDPNEKRDHM VLLEFVTAAG ITLGMDELYK GGTGGSMSKG EELFTGVVPI LVELDGDVNG
421 HKFSVRGEGE GDATNGKLTL KFICTTGKLP VPWPTLVTTL TYGVQCFSRY PDHMKQHDFF
481 KSAMPEGYVQ ERTISFKDDG TYKTRAEVKF EGDTLVNRIE LKGIDFKEDG NILGHKLEYN
541 WNANLAPNLP TAYVKDQITL DFAYWAKNGP AIATRWNEWL VKLQVDEQKL ISEEDLNAVG
601 QDTQEVIVVP HSLPFKVVVI SAILALVVLT IISLIILIML WQKKPR*
```

iGABASnFR2

```
  1 METDTLLLWV LLLWVPGSTG DRSESINFVS WGGSTQDAQK QAWADPFSKA SGITVVQDGP
 61 TDYGKLKAMV ESGNVQWDVV DVEADFALRA AAEGLLEPLD FSVIQRDKID PRFVSDHGVG
121 AFLYSYVLGY NEGKLGASKP QDWTALFDTK TYPGKRALYK WPSPGVLELA LLADGVPADK
181 LYPLDLDRAF KKLDTIKKDI VWWGGGAQSQ QLLASGEVSM GQFWNGRIHA LQEDGAPVGV
241 SWKQNLVMAD ILVVPKGTKN KAAAMKFLAS ASSAKGQDDF SALTAYAPVN IDSVQRLDLA
301 QVRITADKQK NGIMANFKIR HNVEDGSVQS ADHYQQNTPI GDGPVLLPDN HYLSTQSVLS
361 KDPNEKRDHM VLLEFVTAAG ITLGMDELYK GGTGGSMSKG EELFTGVVPI LVELDGDVNG
421 HKFSVRGEGE GDATNGKLTL KFICTTGKLP VPWPTLVTTL TYGVQCFSRY PDHMKQHDFF
481 KSAMPEGYVQ ERTISFKDDG TYKTRAEVKF EGDTLVNRIE LKGIDFKEDG NILGHKLEYN
541 WNANLAPNLP TAYVKDQITL DFAYWAKNGP AIATRWNEWL VKLQVDEQKL ISEEDLNAVG
601 QDTQEVIVVP HSLPFKVVVI SAILALVVLT IISLIILIML WQKKPR*
```

iGABASnFR2n

```
  1 METDTLLLWV LLLWVPGSTG DRSESINFVS WGGSTQDAQK QAWADPFSKA SGITVVQDGP
 61 TDYGKLKAMV ESGNVQWDVV DVEADFALRA AAEGLLEPLD FSVIQRDKID PRFVSDHGVG
121 AFLFSHVLGY NEGKLGASKP QDWTALFDTK TYPGKRALYK WPSPGVLELA LLADGVPADK
181 LYPLDLDRAF KKLDTIKKDI VWWGGGAQSQ QLLASGEVSM GQFWNGRIHA LQEDGAPVGV
241 SWKQNLVMAD ILVVPKGTKN KAAAMKFLAS ASSAKGQDDF SALTAYAPVN IDSVQRLDLA
301 QVRITADKQK NGIMANFKIP HNVEDGSVQL ADHYQQNTPI GDGPVLLPDN HYLSTQSVLS
361 KDPNEKRDHM VLLEFVTAAG ITLGMDELYK GGTGGSMSKG EELFTGVVPI LVELDGDVNG
421 HKFSVRGEGE GDATNGKLTL KFICTTGKLP VPWPTLVTTL TYGVQCFSRY PDHMKQHDFF
481 KSAMPEGYVQ ERTISFKDDG TYKTRAEVKF EGDTLVNRIE LKGIDFKEDG NILGHKLEYN
541 WNANLAPNLP TAYVKDQITL DFAYWAKNGP AIATRWNEWL VKLQVDEQKL ISEEDLNAVG
601 QDTQEVIVVP HSLPFKVVVI SAILALVVLT IISLIILIML WQKKPR*
```

Figure 2. Characterization of iGABASnFR variants in cultured neurons.

a. Fluorescence images of primary neurons expressing iGABASnFR1 (orange), iGABASnFR2 (green), iGABASnFR2n (blue) under the CAG promoter at baseline, at peak brightness after field stimulation with 40 APs, and the corresponding ΔF/F0. Scale bar, 20 μm.

b. Time courses of the ΔF/F0 response to 1, 10 and 40 APs delivered at 83 Hz. iGABASnFR2n signals are inverted for display. Traces and error bars denote mean ± s.e.m., n = 20 culture wells for each variant.

c. 10–90% rise time of the three sensor variants for the 1 AP condition.

d. Peak ΔF/F0 of the three variants over different levels of stimulation.

e. Signal-to-noise (d′) of the three variants over different levels of stimulation.

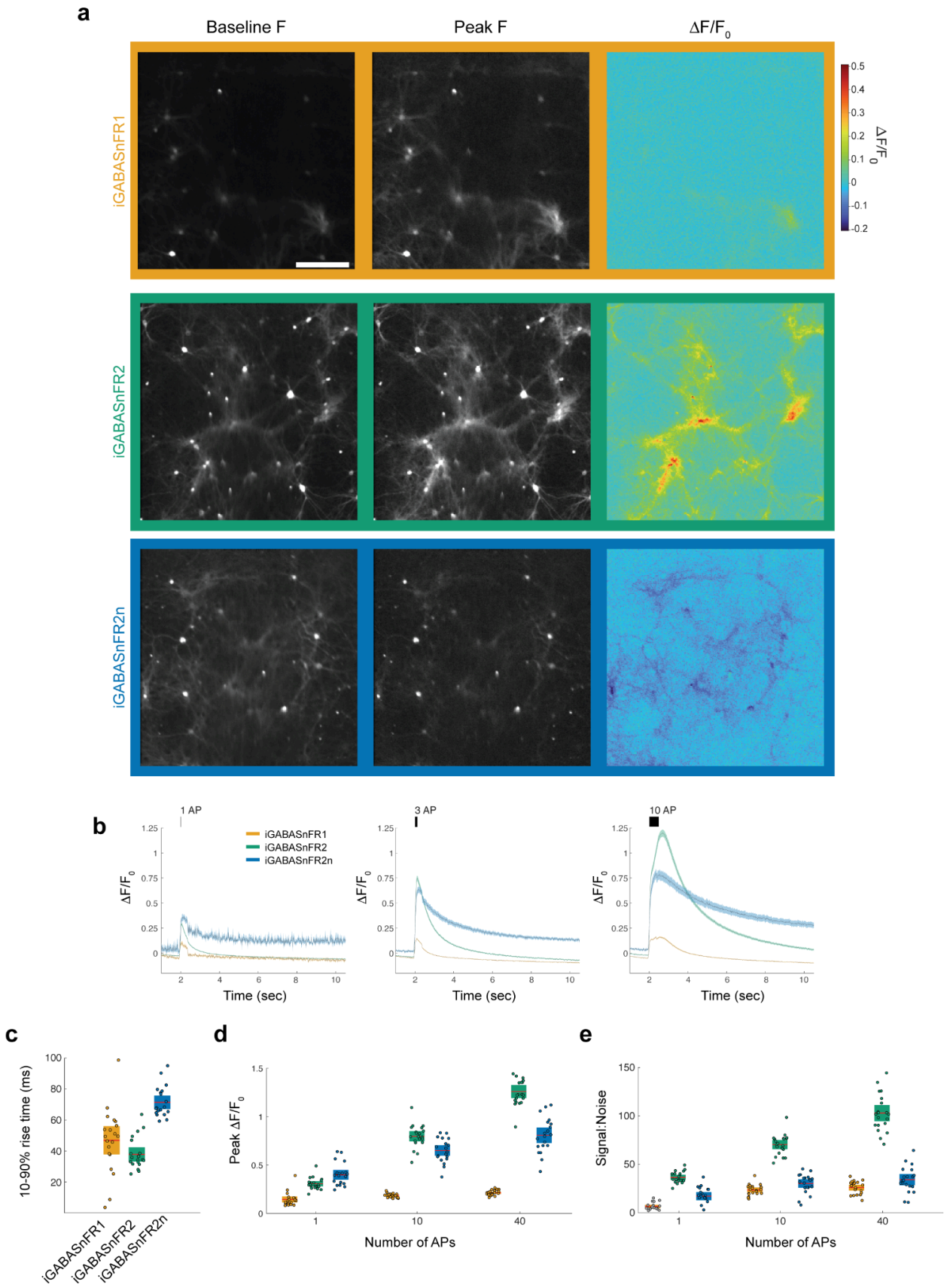
a
Baseline F
Peak F
ΔF/F0
iGABASnFR1
iGABASnFR2
iGABASnFR2n
ΔF/F0
b
1 AP
3 AP
10 AP
iGABASnFR1
iGABASnFR2
iGABASnFR2n
ΔF/F0
Time (sec)
c
10-90% rise time (ms)
iGABASnFR1
iGABASnFR2
iGABASnFR2n
d
Peak ΔF/F0
Number of APs
e
Signal:Noise
Number of APs

Figure 3. Crystal structure of iGABASnFR2 in complex with GABA

a. Superposition of the structure of iGABASnFR2 in complex with GABA (cyan) and unliganded iGABASnFR precursor (magenta). The bound GABA molecule is represented as colored spheres.

b. Cartoon representation of iGABASnFR2 with key mutations shown as yellow sticks. Mutations in the original iGABASnFR1 shown in orange.

c. GABA binding site of iGABASnFR2. Residues involved in GABA binding are shown as lines and GABA shown as stick.

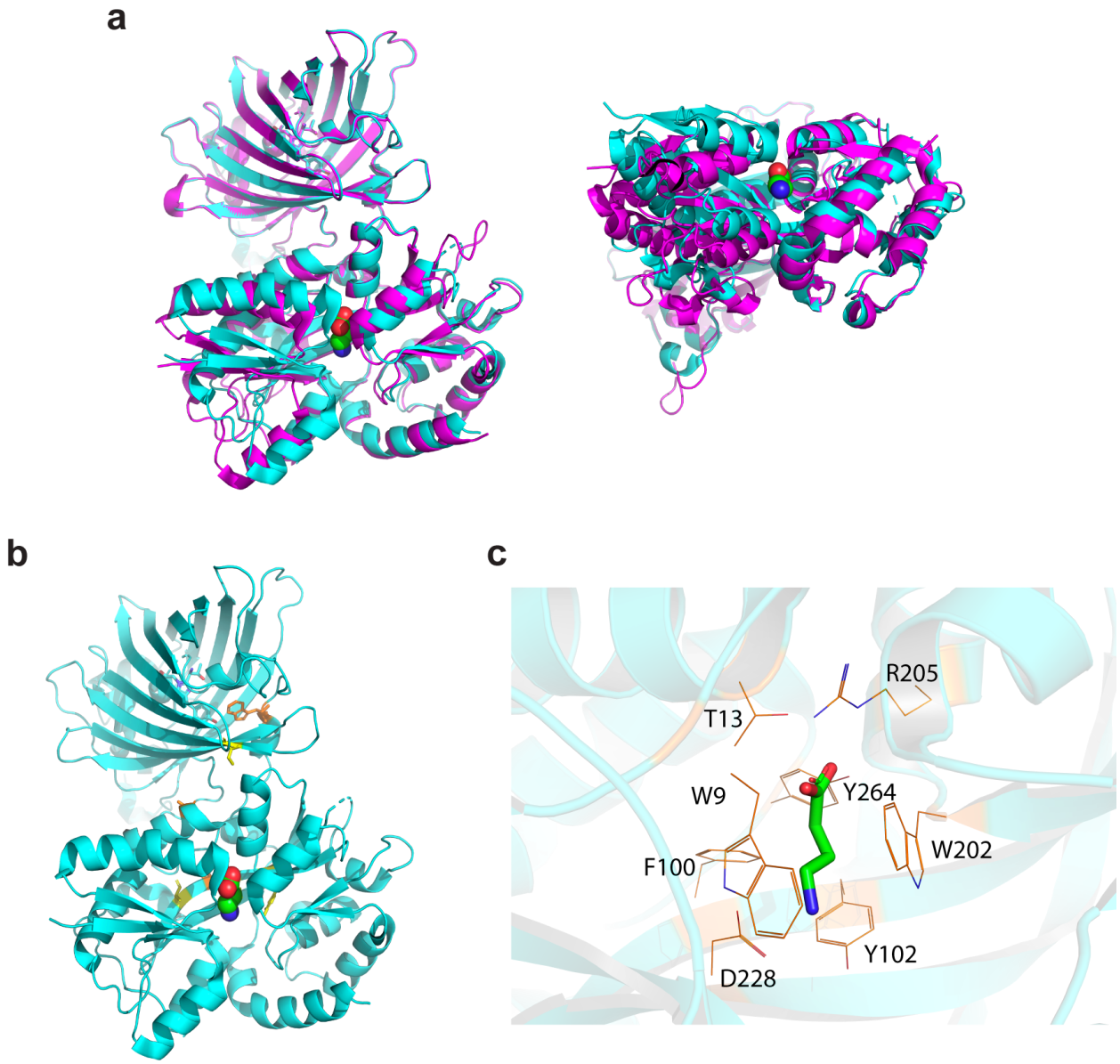

Figure 3 Supplementary Table 1: Data collection and refinement statistics of iGABASnFR2 in complex with GABA.

	iGABASnFR2+GABA
Data collection	
Space group	P1 2_1 1
Cell dimensions	
a, b, c (Å)	76.5, 109.9, 214.3
α, β, γ (°)	90.00, 100.3, 90.00
Resolution (Å)	48.74-2.60 (2.64-2.60)
R_{merge}	0.067 (0.434)
Mean ((I)/sd(I))	11.0 (2.6)
Completeness %	98.5 (99.9)
Multiplicity	3.6 (3.8)
Refinement	
Resolution	47.39-2.60
No. reflections all/free	105768/5396
R_{work}/R_{free}	0.249/0.206
No. atoms	
Protein	24386
Ligand	174
Water	32
B-factor (Å)	
Protein	50.64
Ligand	41.32
Water	35.23
R.M.S. deviations	
Bond lengths (Å)	0.007
Bond angles (°)	1.610

Figure 4. Biophysical properties of iGABASnFR variants.

a. GABA titrations with purified iGABASnFR protein. Lines indicate fits to mean of n = 5 titration series, error bars are s.e.m.

b. GABA titrations with sensors expressed on the surface of cultured neurons. Fits (bottom panel) show ΔF/F0 response to increasing concentrations of GABA measured with ROIs placed on individual cell bodies (top panel). In these conditions iGABASnFR2 shows a greater dynamic range than iGABASnFR1, in contrast to results with purified protein. Color lookup table is the same for all images. Scale bar: 50 μm. Illumination: 5.6 mW/mm^2, imaging at 1 frame per sec.

c. Observed reaction rate constant (K_{obs}) values from stopped-flow measurements for the three sensors.

d. Stopped flow kinetics of iGABASnFR variants. Lines indicate fits to mean of n = 3 replicates from three separate batches of purified protein.

e. One-photon excitation and emission spectra of soluble iGABASnFR protein in the presence (10 mM) and absence of GABA.

f. Two-photon excitation spectra and the computed ΔF/F0 of iGABASnFR variants in the presence (10 mM) and absence of GABA.

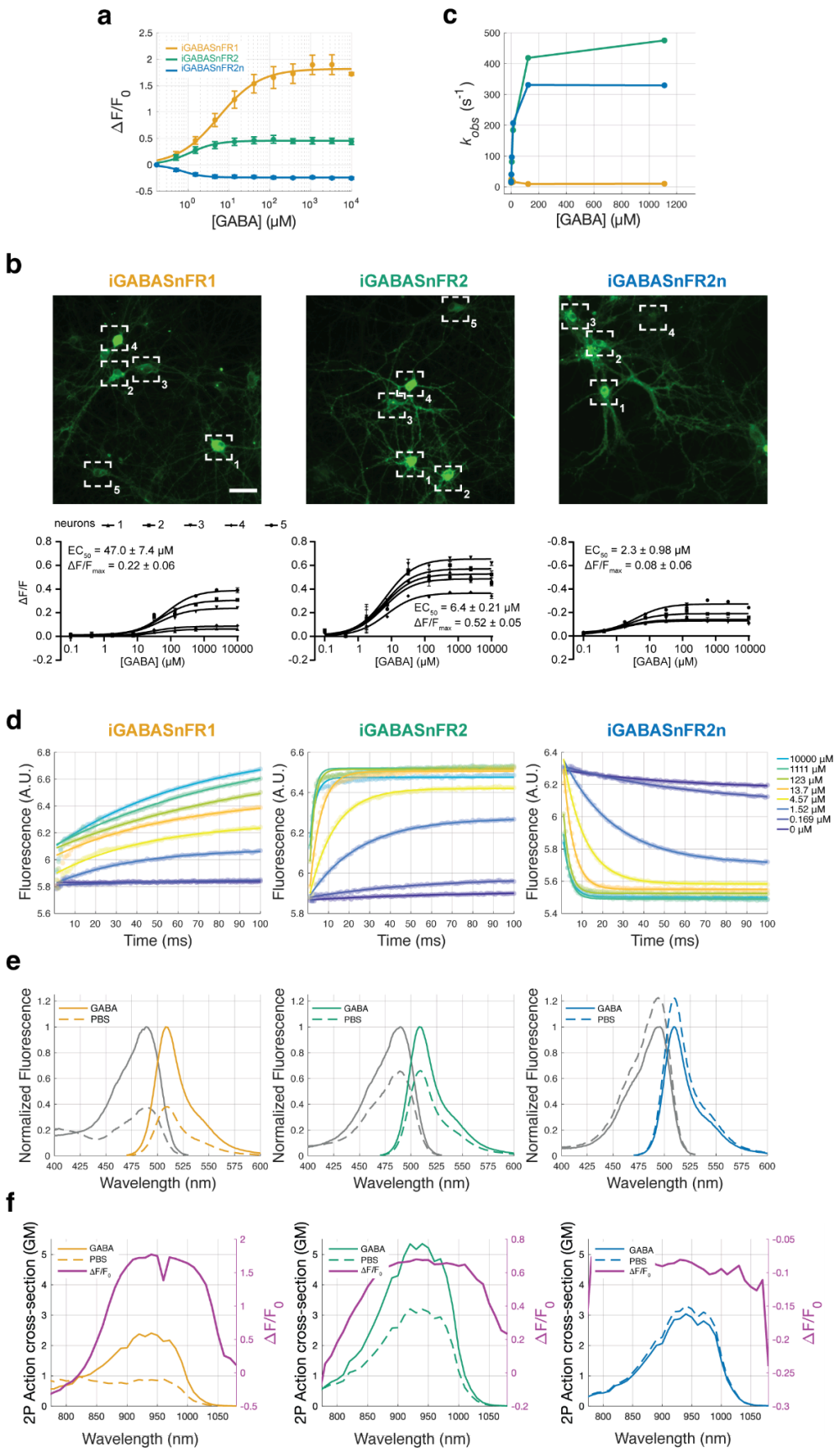
a
iGABASnFR1
iGABASnFR2
iGABASnFR2n
ΔF/F0
[GABA] (μM)
c
kobs (s-1)
[GABA] (μM)
b
iGABASnFR1
iGABASnFR2
iGABASnFR2n
neurons 1 2 3 4 5
EC50 = 47.0 ± 7.4 μM
ΔF/Fmax = 0.22 ± 0.06
EC50 = 6.4 ± 0.21 μM
ΔF/Fmax = 0.52 ± 0.05
EC50 = 2.3 ± 0.98 μM
ΔF/Fmax = 0.08 ± 0.06
ΔF/F
[GABA] (μM)
d
iGABASnFR1
iGABASnFR2
iGABASnFR2n
Fluorescence (A.U.)
Time (ms)
10000 μM
1111 μM
123 μM
13.7 μM
4.57 μM
1.52 μM
0.169 μM
0 μM
e
GABA
PBS
Normalized Fluorescence
Wavelength (nm)
f
GABA
PBS
ΔF/F0
2P Action cross-section (GM)
Wavelength (nm)

Figure 4 - figure supplement 1. Responses of iGABASnFR variants to GABA-related compounds.

Different iGABASnFR variants (200 nM) were titrated with various concentrations of ligands of interest. Estimated EC_{50} values shown in insets. Each titration has a minimum of n=1 replicate.

Figure 4 - figure supplement 2. pH titrations of iGABASnFR variants.
Fluorescence response of the three iGABASnFR variants across a pH titration, under GABA-saturated (10 mM, solid lines) and GABA-free (dashed lines) conditions. Fluorescence values are normalized to the peak fluorescence of the GABA-saturated form of each sensor. Measurements were performed using 200 nM sensor concentration. Data points represent the mean of n = 3 technical replicates; error bars indicate s.e.m.

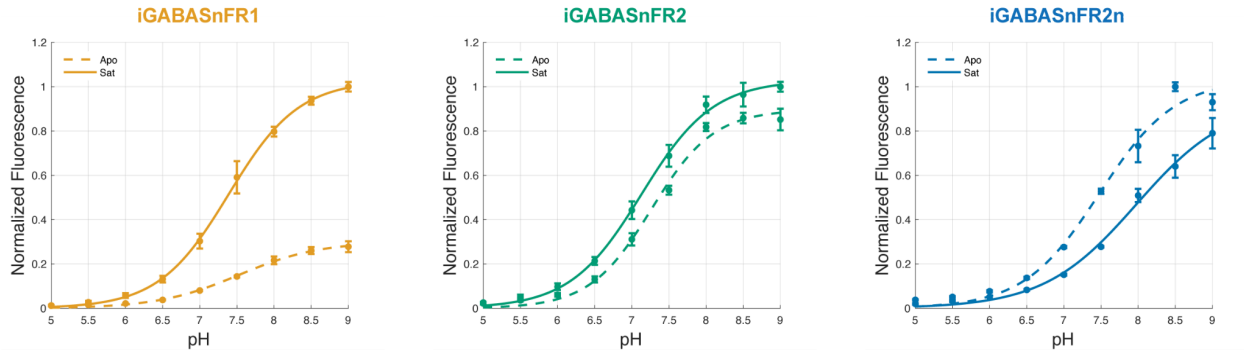

Figure 5. iGABASnFR2 reports direction selectivity in the retina

a. Schematic illustration of centrifugal direction selectivity in starburst cell's motion responses.

b. Spatially asymmetric inhibitory connections (red dots) between starburst cells (SACs) and direction-
selective ganglion cells (DSGCs), which are proposed to generate direction selectivity in DSGCs.

c. Example field of view of SAC processes expressing iGABASnFR1. Yellow region of interest (ROI) is analyzed to evaluate responses to visual stimuli.

d. Responses to static flash from ROI in **c** but with SACs expressing iGABASnFR2.

e. Responses to motion stimulus.

f-h. Results of imaging using iGABASnFR2.

i. Histograms of response amplitude index (left) and response reliability (right) from SACs expressing iGABASnFR. n = 147 ROIs collected across 5 retinae.

j. As in **i** but with SACs expressing iGABASnFR2. n = 346 ROIs collected from 3 retinae. Responses to motion stimulus.

k. Average signals during preferred direction motion with iGABASnFR1 (top, gray) and iGABASnFR2 (bottom, cyan). Line and shading indicate mean ± s.d (n = 147 for iGABASnFR, n = 346 for iGABASnFR2).

l. Comparison of SNR of the motion response detected with the two sensor versions. p = 0. Two-tailed Mann-Whitney-Wilcoxon test.

m. Comparison of direction selectivity (CV, circular variance) for the two sensor versions. $p = 7.812 \times 10^{-6}$. Two-tailed Mann-Whitney-Wilcoxon test.

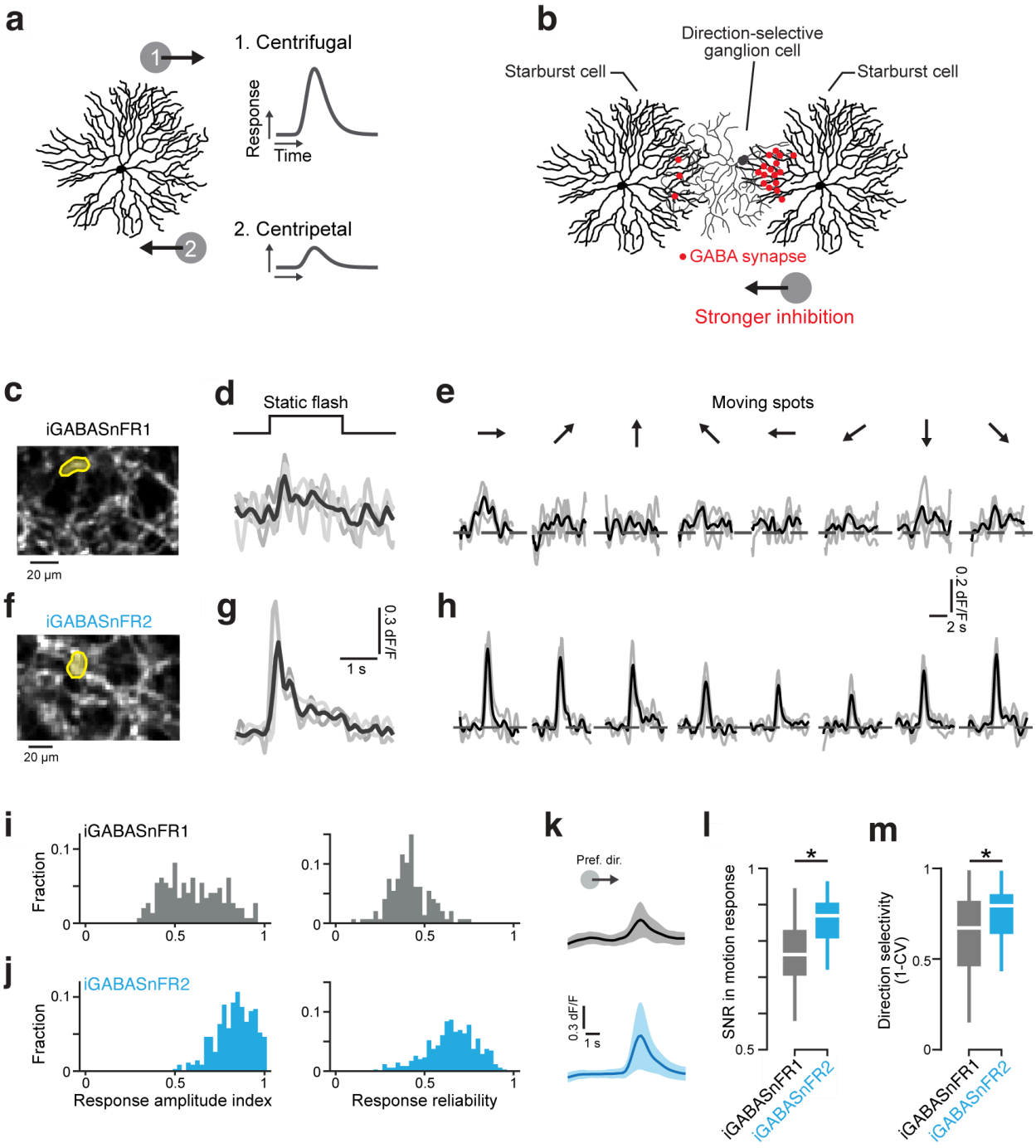
a
1. Centrifugal
Response
Time
2. Centripetal
b
Direction-selective ganglion cell
Starburst cell
Starburst cell
GABA synapse
Stronger inhibition
c
iGABASnFR1
20 µm
d
Static flash
e
Moving spots
0.2 dF/F
2 s
f
iGABASnFR2
20 µm
g
0.3 dF/F
1 s
h
i
iGABASnFR1
Fraction
0.1
0
0
0.5
1
j
iGABASnFR2
Response amplitude index
Response reliability
k
Pref. dir.
0.3 dF/F
1 s
l
SNR in motion response
1
0.5
*
iGABASnFR1
iGABASnFR2
m
Direction selectivity (1-CV)
1
0.5
0
*
iGABASnFR1
iGABASnFR2

Table 1: Photophysical properties of iGABASnFR variants as purified proteins

	λ_{abs} (nm)	λ_{Ex} (nm)	λ_{Em} (nm)	ΔF/F	ε (M/cm^2)		Φ		τ (ns)	
					GABA	PBS	GABA	PBS	GABA	PBS
iGABASnFR1	490	489	508	1.9	14070 ± 600	5375 ± 220	0.58 ± 0.01	0.54 ± 0.03	2.22 ± 0.05	2.32 ± 0.01
iGABASnFR2	490	490	508	0.46	26195 ± 390	19800 ± 380	0.61 ± 0.02	0.54 ± 0.01	2.29 ± 0.08	2.30 ± 0.02
iGABASnFR2n	493	496	509	-0.13	12390 ± 690	13000 ± 220	0.72 ± 0.02	0.76 ± 0.01	2.71 ± 0.02	2.72 ± 0.02